AIAA JOURNAL
Vol. 34, No. 12, December 1996

Engineering Estimation of Fluctuating Loads in Shock Wave/Turbulent Boundary-Layer Interactions

L. Brusniak* and D. S. Dolling†
University of Texas at Austin, Austin, Texas 78712-1085

In an earlier experimental study of the flow upstream of a blunt fin in a Mach 5 turbulent boundary layer, the authors showed that the low-frequency (below 4 kHz) component of the fluctuating wall pressures can be attributed largely to an instantaneous pressure distribution $\mathcal{P}_i$, which expands and contracts as its upstream boundary translates aperiodically between the upstream influence and separation lines. Based on the physical similarity between $\mathcal{P}_i$ and the time-averaged (mean) wall pressure distribution, the authors demonstrated the feasibility of predicting fluctuating pressure loads using mean wall pressure distributions obtained from either computation or experiment. The objective of the present study was to determine whether the approach is applicable to a broader range of flows involving shock wave/turbulent boundary-layer interaction. For all cases examined, the locations of local maxima and minima in the measured wall pressure standard deviation distributions were estimated correctly. Further, quantitatively accurate estimates of the magnitude of fluctuating wall pressure and heat transfer levels were obtained using the corresponding time-averaged distributions. The most critical factors affecting the accuracy of the estimates appear to be the shape of the instantaneous pressure (heat transfer) distribution and the length of shock foot motion.

Introduction

THE interaction of shock waves with turbulent boundary layers can pose significant problems in the design of high-speed vehicles.[1] When the flow is separated, large fluctuating pressure loads of up to 185 dB or more[2] can occur and can have characteristic frequencies close to the resonant frequencies of vehicle structural components.[3] In addition, the attendant high heating rates can further threaten the structural integrity of vehicle components. Interactions can arise from a variety of sources such as surface protuberances (wing–body junctures, antennae), abrupt turning of the high-speed flow (engine inlets, deflected elevons), and incident shocks originating from other parts of the vehicle. A number of experimental studies have been made of the surface pressure fluctuations under separated and unseparated interactive flows generated by compression corners, ogive-cylinder cone-frustum configurations, blunt and sharp fins, cylinders, and incident shocks. Dolling[2] provides an extensive review of most of these experiments. The authors are also aware of one example of measurements of fluctuating heat transfer levels associated with incident shock interactions.[4]

Figure 1 highlights some of the significant features of separated flows for the case of a hemicylindrically blunted fin of leading-edge diameter D. In this example, in which the interaction size is controlled mainly by D, there is a large-scale, three-dimensional, vortical, separated flowfield that, as is typically the case for shock-induced turbulent separation, is highly unsteady. The unsteadiness is most visibly associated with the foot of the separation shock, which undergoes aperiodic motion over a streamwise length of order D, between the upstream-influence line (UI) and the separation line (S, deduced using surface tracer flow visualization techniques[5–8]). The effect of the unsteady shock is clearly visible in the wall-pressure signal of Fig. 1, which is characterized by a low-amplitude, high-frequency component associated with the incoming undisturbed turbulent boundary layer, a high-amplitude, low-frequency component due to the intermittent passage of the shock foot over the transducer, and a high-amplitude, high-frequency component associated with the separated flow downstream of the shock foot. The bandwidth of the shock-foot-associated low-frequency component is a few hundred hertz to several kilohertz.[2]

The goal of many recent studies has been not only to document the load levels associated with the unsteadiness but also to determine the causes of the unsteadiness in the hope that methods for predicting the unsteady aspects of the flowfield can be developed. The analytical models of Keefe and Nixon[9] and Debieve and Lacharme,[10] for example, take advantage of the characteristic pressure jump across the moving shock (see Fig. 1) and model it as a step function. This approach appears to be physically reasonable for modeling the characteristics of the fluctuating pressures in the region of shock motion

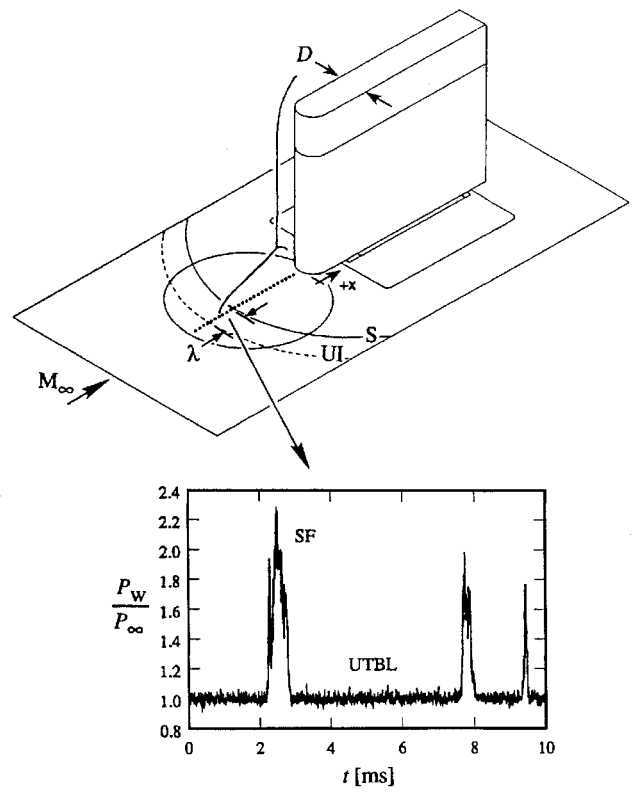

Fig. 1 Blunt fin flowfield.

Received Oct. 14, 1995; revision received Aug. 20, 1996; accepted for publication Aug. 23, 1996; also published in *AIAA Journal on Disc*, Volume 2, Number 1.

*Postdoctoral Fellow, Applied Research Laboratories. Member AIAA.
†Professor, Department of Aerospace Engineering and Engineering Mechanics. Associate Fellow AIAA.

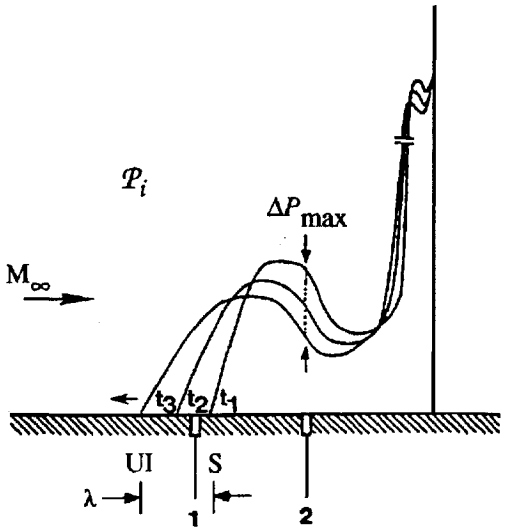

Fig. 2a $\mathcal{P}_i$ distribution.

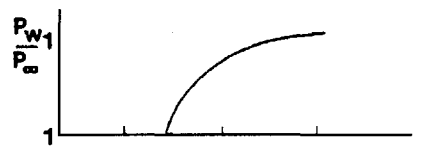

Fig. 2b Pressure–time variation at station 1 for shock foot upstream sweep.

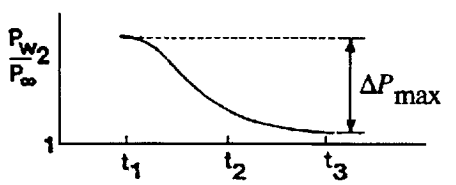

Fig. 2c Pressure–time variation at station 2 for shock foot upstream sweep.

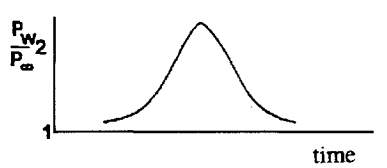

Fig. 2d Pressure–time variation at station 2 for shock foot downstream-to-upstream turnaround.

(i.e., between UI and S), but inappropriate for the remainder of the flow, where the pressure signals lack such distinctive features. Other methods have used the available database to develop correlations (e.g., Ref. 11).

Recent experimental studies at Mach 5 using blunt fins have provided additional insight into the physical characteristics of the pressure fluctuations from downstream of S to the fin root.[6,12] In particular, Brusniak and Dolling[12] showed that the low-frequency (below about 4 kHz) content of fluctuating pressures measured at any station (on centerline) and the characteristics of two-point correlations between any two measurement stations are due to an instantaneous pressure distribution $\mathcal{P}_i$, which expands and contracts as its upstream boundary translates aperiodically between the upstream-influence and separation lines. The concept is illustrated in Fig. 2a for a hypothetical shock foot upstream sweep from S to UI. The $\mathcal{P}_i$ distribution is shown at three instants in time and, as sketched, stretches and flattens during the sweep. Figures 2b and 2c show the resulting pressure variations sensed at the wall at the two corresponding stations shown in Fig. 2a. At time t_1 the pressure at station 1 is initially at the undisturbed freestream level because the shock foot is still downstream of it. As time progresses, the pressure level rises rapidly owing to the passage of the upstream edge of $\mathcal{P}_i$ over station 1. At station 2, the pressure is initially at its highest level since the upstream edge of $\mathcal{P}_i$ is at S (t_1). As time progresses and the shock foot moves upstream, $\mathcal{P}_i$ translates and flattens, resulting in a decrease in pressure with time at station 2. At time t_3 the pressure at station 2 is at its lowest level since the leading edge of $\mathcal{P}_i$ is at UI. The total change in pressure sensed at station 2 (ΔP_{max} in Figs. 2a and 2c) is the difference between the pressure levels at times t_1 and t_3. In the case where the shock foot is initially traveling in the downstream direction and then reverses direction, a rise and then fall in pressure will be measured at station 2 (Fig. 2d). In these examples, the statistical variance of the fluctuating pressure level measured at a point is clearly due to the local changes in pressure that occur as $\mathcal{P}_i$ moves about. Note also from Fig. 2a that the value of ΔP_{max} varies between stations 1 and 2 and has a minimum value at some point between these two stations. This minimum value will be evident as a local minimum in the fluctuating pressure standard deviation distribution.

The significance of the preceding result is that, knowing $\mathcal{P}_i$, and the physical extent of the expansion/contraction of $\mathcal{P}_i$, it should be possible to develop methods that can predict the surface loading throughout the entire flowfield. The question now arises: How can $\mathcal{P}_i$ be determined? As seen by comparing the $\mathcal{P}_i$ distributions in Fig. 2a to the experimentally measured time-averaged pressure distribution in Fig. 3a, each $\mathcal{P}_i$ distribution bears a close resemblance to $\bar{P}_W(x)$ (also see Figs. 4 and 13 of Ref. 12 for examples of experimentally measured $\mathcal{P}_i$ and $\bar{P}_W$ distributions). Using this observation, Brusniak and Dolling[12] raised the possibility that, if computational solutions of the mean wall pressure distribution correspond to a particular $\mathcal{P}_i$ distribution (i.e., at a given instant in time), then it may be possible to calculate a series of $\mathcal{P}_i$ distributions by solving for the flowfield with different incoming boundary conditions such that the separation shock foot was fixed at several stations spanning the region of shock motion. Alternatively, a simpler approach would be to use a single mean pressure distribution, obtained from experiment or computation, to approximate the spatial distribution of $\mathcal{P}_i$. Using the latter approach, Brusniak and Dolling[12] were able to predict most of the key features of the wall pressure standard deviation distribution on centerline upstream of a blunt fin at Mach 3. In light of this apparent success (which, incidentally, represented only a single application of the idea), the next logical step is to further develop the method and apply it to a wide variety of turbulent interactive flows to determine 1) how well the method works, 2) the validity of simplifying assumptions, and 3) any additional factors that may need to be considered. Thus, the objective of this study is to evaluate the general applicability of Brusniak and Dolling's method to a broad range of separated flows arising from shock wave/turbulent boundary-layer interactions. The ultimate goal is to provide designers a physically meaningful, simple tool for obtaining first-order estimates of the location and magnitude of dynamic surface loads.

Background

Before describing the method, this section discusses the extent to which different frequency bands contribute to measured wall pressure standard deviation values. Figures 3a and 4a show the mean pressure distributions on centerline for blunt fin and compression ramp induced turbulent separation at Mach 5 (the data are from Refs. 13 and 14, respectively). Figures 3b and 4b show the corresponding standard deviation distributions. As described by Brusniak and Dolling,[12] the large-amplitude, low-frequency pressure fluctuations (below about 4 kHz for their blunt fin case) are due to $\mathcal{P}_i$. Thus, the original time series data used to obtain Figs. 3 and 4 (with a bandwidth of 50 kHz) were filtered using a finite impulse response digital filter (4096 point, Hamming windowed data) at a low-pass cutoff frequency f_c of 7 kHz, giving the distributions indicated in Figs. 3b and 4b as σ_{LP}. The corresponding highpass filtered results are also shown in the figures (σ_{HP}). At the upstream end of the interactions the standard deviation distributions are generated almost entirely by frequencies below 7 kHz. In the downstream direction, although the contribution from low frequencies decreases, the shape of $\sigma_{LP}(x)$ undergoes characteristic variations (especially in Fig. 3b),

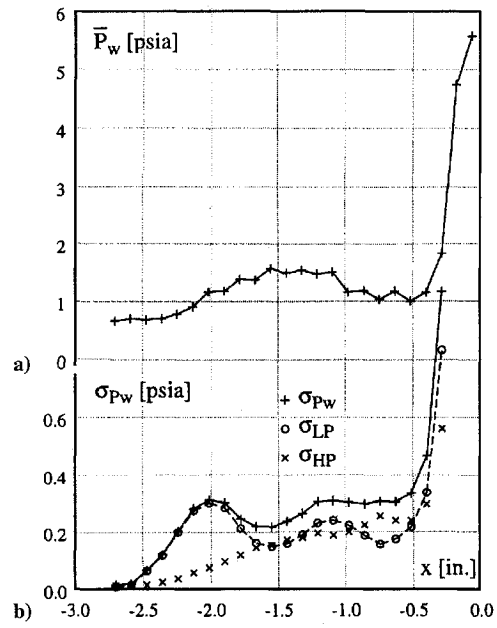

Fig. 3 Mach 5 blunt fin centerline a) mean pressure distribution and b) standard deviation distributions.

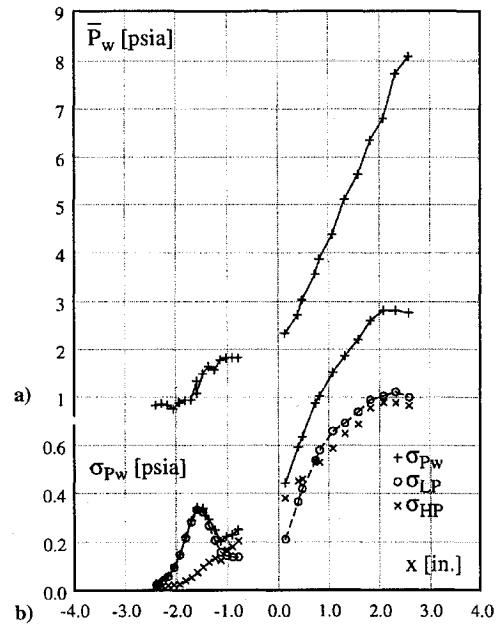

Fig. 4 Mach 5 compression ramp streamwise a) mean pressure distribution and b) standard deviation distributions.

whereas the high-frequency contribution $[\sigma_{HP}(x)]$ simply increases continuously. An additional point is that the qualitative character of the $\mathcal{P}_i$-associated standard deviation distributions $[\sigma_{LP}(x)]$ can be inferred from the character of the mean pressure distribution: regions of local maxima and minima in $\sigma_{Pw}(x)$ will essentially correspond to regions of local maxima and minima, respectively, in the slope of the mean pressure distribution.[12] This relationship can be seen in Figs. 3 and 4. One last point is that the low-frequency estimates $[\sigma_{LP,est}(x)]$ obtained in the cases that follow will correspond to the low-frequency-associated contributions to $\sigma_{Pw}(x)$ [i.e., $\sigma_{LP,est}(x) \approx \sigma_{LP}(x)$], which in general are the basic frequencies of concern to designers.[3] Since the high-frequency $[\sigma^2_{HP}(x)]$ contribution to the overall variance is not modeled in the method, the expectation is that $\sigma_{LP,est}(x) < \sigma_{Pw}(x)$, with the smallest differences between these two quantities occurring at the upstream portion of the interaction where the highest loads at low frequency occur.

In experimental studies, the variance, $\sigma^2_{Pw}(x)$, can be obtained (by definition) by integrating the power spectrum from the minimum frequency f_m, to the maximum frequency f_M (the analog filter low-pass cutoff frequency used in the experiments). Given that the digital filter cutoff frequency lies between f_m and f_M, that f_m is small enough so that practically all of the low-frequency portion of the power spectrum (the portion associated with large-scale shock motion) is included, and that f_M is large enough so as to capture the high-frequency content well above that associated with the low-frequency shock motion, then $\sigma^2_{Pw}(x)$ can by definition be related to $\sigma_{LP}(x)$ and $\sigma_{HP}(x)$ as $\sigma^2_{Pw} = \sigma^2_{LP} + \sigma^2_{HP}$. As pointed out by one of the reviewers of this paper, the latter is true provided $\tilde{P}_{LP}(x, t)$ and $\tilde{P}_{HP}(x, t)$, the low- and high-frequency components of the signal, are uncorrelated. This is a reasonable assumption.

As discussed earlier, $\sigma_{LP,est}(x)$ will correspond to $\sigma_{LP}(x)$. For the entire flow, the approximation is made that $\sigma_{HP}(x) \approx \sigma_{Pwo}$ (where σ_{Pwo} is the undisturbed level of σ_{Pw} just upstream of the interaction). This is done to match the undisturbed values of σ_{Pwo} from experiment and from $\sigma_{LP,est}(x)$ (the latter would otherwise give values of zero upstream of the interaction). Thus, estimates of $\sigma_{Pw}(\sigma_{Pw,est})$ will be presented as $\sigma_{Pw,est} = \sqrt{(\sigma^2_{LP,est} + \sigma^2_{Pwo})}$ in the results that follow. In most of the cases examined, $\sigma_{Pwo} \ll \sigma_{LP}$ at the upstream portion of the interaction (typically, σ_{Pwo} is from 7.5 to 22 times smaller than the value of the upstream maximum in σ_{Pw}) so that $\sigma_{Pw,est} \approx \sigma_{LP,est}$ there. The increasing difference between σ_{Pw} and $\sigma_{Pw,est}$ with streamwise distance [i.e., $\sqrt{(\sigma^2_{Pw} - \sigma^2_{Pw,est})}$] is due to the increasing contribution of $\sigma^2_{HP}(x)$ to the overall variance (e.g., see Figs. 3b and 4b).

Method

Analysis Assumptions

In this section, several of the assumptions and approximations used in the analysis are discussed. They are not intended to be a fixed set of rules but more of a guide for minimizing possible sources of error.

Existence of $\mathcal{P}_i$

The most fundamental assumption is that a $\mathcal{P}_i$-type distribution does in fact exist for all interactive flows; that is, that low-frequency pressure fluctuations at the surface are due to $\mathcal{P}_i$. The existence of $\mathcal{P}_i$ for blunt fins and compression ramps can be seen from the experimental studies at Mach 5 by Brusniak and Dolling[12] and Erengil and Dolling,[15] respectively, and can be inferred in other cases from the similar character of fluctuating signals from the region of shock motion. This assumption will be essentially validated by the results.

Probability Density Function of Shock Foot Position

The probability density function (PDF) of shock foot location in the region of shock motion (i.e., between UI and S in Fig. 1) is assumed to be Gaussian. This assumption is validated by experimental measurements of streamwise shock foot position–time histories.[16] In this study, the shock foot position–time history is denoted by $x_s(t)$ and the maximum shock foot excursion (the distance between UI and S) is given by λ (see Fig. 1). The standard deviation of $x_s(t)$ is denoted σ_{xs}.

Approximation of $\mathcal{P}_i(x)$ Using Time-Averaged Pressure Distribution $\bar{P}_W(x)$

It is assumed that the shape of the $\mathcal{P}_i$ distribution can be approximated using the time-averaged distribution, that is, that $\mathcal{P}_i(x) \approx \bar{P}_W(x)$ and that $\bar{P}_W(x)$ represents $\mathcal{P}_i(x)$ when the shock foot is at its most probable location. Consequently, $\mathcal{P}_i$ is assumed to be constant in space, independent of shock foot location (i.e., that it translates only and does not undergo the observed expansion and contraction illustrated in Fig. 2a). Thus, this simplified model employs a type of frozen flow assumption.

Not knowing the shape of $\mathcal{P}_i(x)$ a priori, it is difficult to establish the accuracy of the approximation for a given $\bar{P}_W(x)$ distribution. The analytical approach suggested by one of the reviewers of this paper, which is outlined below and culminates in Eq. (2), provides some insight into this issue. By fixing the shock foot location x_s of the actual $\mathcal{P}_i$ distribution at its mean location $\bar{x}_s$ (which is also the most probable location due to the assumed PDF of shock foot location), the instantaneous wall pressure at time t and station x due to $\mathcal{P}_i$ can be calculated as $P_W(x, t) = \mathcal{P}_i(x - \Delta x) = \mathcal{P}_i[x - \lambda d(t)]$.

Here, Δx represents shock foot displacement from $\bar{x}_s$ and is given by $\Delta x = \lambda d(t)$, where λ is the length of the region of shock foot motion and d is a Gaussian random variable with zero mean and variance σ_d^2. (These parameters are discussed further in the Implementation of Method section.) Now, by expanding $\mathcal{P}_i[x - \lambda d(t)]$ in a Taylor series about the point x and then time averaging, $\bar{P}_W(x)$ can be expressed as

$$\bar{P}_W(x) = \mathcal{P}_i(x) + \frac{\lambda^2\sigma_d^2}{2!}\frac{d^2(\mathcal{P}_i)}{dx^2} + \frac{3\lambda^4\sigma_d^4}{4!}\frac{d^4(\mathcal{P}_i)}{dx^4} + \cdots \quad (1)$$

$$= \mathcal{P}_i(x) + \sum_{m=2,4,6,\ldots}^{\infty} \frac{(\lambda\sigma_d)^m}{m!!}\frac{d^m(\mathcal{P}_i)}{dx^m} \quad (2)$$

where $m!! = 2 \times 4 \times 6 \ldots (m-2) \times (m)$ with m even. Equation (2) represents what would be measured experimentally. When $\lambda = 0$ (steady flow with no shock foot motion), $\bar{P}_W(x) = \mathcal{P}_i(x)$ for all x. When $\lambda \neq 0$, it is not entirely clear how the terms involving derivatives contribute to $\bar{P}_W(x)$ and consequently affect the approximation $\mathcal{P}_i(x) \approx \bar{P}_W(x)$. Although the physical meaning of the factors involving the product $\lambda\sigma_d$ is clear, the behavior of the derivatives of $\mathcal{P}_i$ is not, because they will vary from point to point and case to case. However, from a qualitative perspective, the second derivative of $\mathcal{P}_i(x)$, for example, gives an indication of the local concavity of $\mathcal{P}_i$. If a given segment of $\mathcal{P}_i(x)$ is approximately linear (i.e., has negligible concavity), then all derivatives of second order and higher will be essentially zero and Eq. (2) will reduce to the desired approximation $\mathcal{P}_i(x) \approx \bar{P}_W(x)$. As seen in Fig. 2a, stations 1 and 2 are exposed largely to local segments of $\mathcal{P}_i(x)$, which are essentially linear. Thus, the value of $\bar{P}_W(x)$ will be essentially equal to $\mathcal{P}_i(x)$ over given intervals about the respective stations. On the other hand, if a given segment of $\mathcal{P}_i(x)$ is nonlinear, the higher-order derivative terms in Eq. (2) will contribute to some extent to the calculated value of $\bar{P}_W(x)$ and the approximation will be less accurate. Consider the concave portion of $\mathcal{P}_i$ between stations 1 and 2 in Fig. 2a. Clearly, if the local concavity of $\mathcal{P}_i$ increases, the second term in Eq. (1) will contribute increasingly to the calculated value of $\bar{P}_W(x)$ and the shape of $\bar{P}_W(x)$ will deviate increasingly from the shape of $\mathcal{P}_i(x)$. The magnitude of the second and higher terms will depend on the size of the factors $[(\lambda\sigma_d)^m/m!!]$ and $[d^m(\mathcal{P}_i)/dx^m]$ in Eq. (2) relative to each other.

As will be evident in the results that follow (see also Ref. 12), local maxima in the wall pressure standard deviation distribution will occur near stations 1 and 2 in Fig. 2a (owing to the linear portions of $\mathcal{P}_i$ with large, nonzero slope), and a local minimum will occur between these two stations (owing to the concave portion of $\mathcal{P}_i$, which has portions with small slope). Since the main objective is to determine the magnitude of local maxima in the pressure standard deviation distribution, the approximation $\mathcal{P}_i(x) \approx \bar{P}_W(x)$ will be valid for calculating the magnitudes of the maxima when $\mathcal{P}_i(x)$ and, hence, $\bar{P}_W(x)$ are linear.

One final note is that the accuracy of the approximation $\mathcal{P}_i(x) \approx \bar{P}_W(x)$ will be affected by the length of shock motion [λ in Eq. (2)]. For a given $\mathcal{P}_i$ distribution, the time-averaged pressure at a point x will be a function of the shape of $\mathcal{P}_i$ over the interval $[-\lambda/2, \lambda/2]$ centered about x. In Fig. 5, $\mathcal{P}_i$ is approximately linear over the interval. If λ is increased (as in the figure), the effect of nonlinearities in $\mathcal{P}_i(x)$ will contribute increasingly to the calculated value of $\bar{P}_W$ and increase the difference between $\bar{P}_W$ and $\mathcal{P}_i$ at station x. This is also evident in Eq. (2), where increasing λ by a factor of m increases the contribution of the second and higher-order derivative terms by factors of m^2, m^4, m^6, and so on (e.g., a doubling of λ increases the contribution of the second term by a factor of $2^2 = 4$). In terms of experimental data, specific areas of concern are regions where very large gradients in the mean distribution occur, such as near the root of blunt fins (Fig. 3a). In such regions, it is difficult to measure the mean pressure distribution accurately, due to finite transducer sizes or wall tapping diameter, and due to minor variations in flow structure from test to test.

Length of Shock Foot Motion

The last issue is the length of the shock foot (and hence $\mathcal{P}_i$) motion. From the wide variety of studies involving two-dimensional interactions (see Ref. 2), the region of shock motion is seen to have a length of shock motion λ of order δ_o, the undisturbed turbulent boundary-layer thickness. That is, $\lambda \approx \delta_o$. For the three-dimensional interaction generated by hemicylindrically blunted fins of leading-edge diameter D, the interaction size depends primarily on D and to a lesser extent on δ_o.[7,8] In these studies, it was found that λ is of order D and will therefore be approximated as $\lambda \approx D$. Note that even though these choices of length of shock foot motion may be entirely appropriate for the upstream portion of the interaction (the region of shock motion), they may be less accurate away from this region (e.g., at the blunt fin root, where $\lambda = 0$).

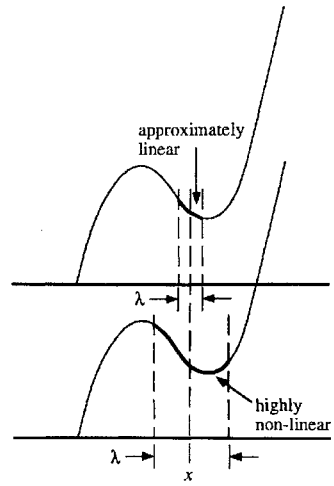

Fig. 5 Effect of λ on measured mean pressure at station x.

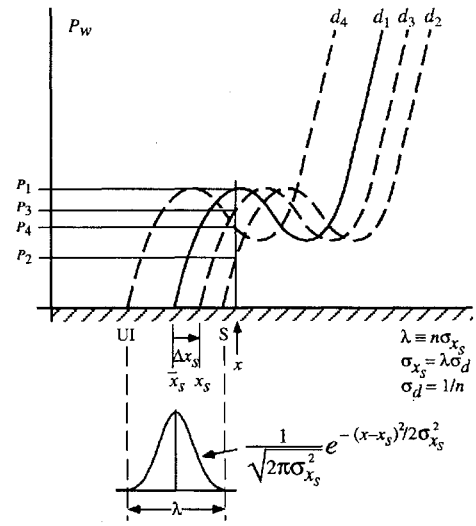

Fig. 6 Illustration of method.

Implementation of Method

This section illustrates how the method is implemented conceptually. Figure 6 shows an example $\mathcal{P}_i$ distribution (solid line) with the shock foot at its mean location $\bar{x}_s$. Also shown is the assumed shock foot location PDF. As discussed earlier, the PDF is taken to be Gaussian, with standard deviation σ_{xs}. Note that, due to the assumed PDF, $\bar{x}_s$ is the most probable shock foot location and is midway between UI and S. The distance λ is taken to be some multiple n of σ_{xs} (i.e., $\lambda = n\sigma_{xs}$). For this study, the value $n = 6$ was used because, for a Gaussian PDF of shock foot location, the probability that x_s is within $\pm 3\sigma_{xs}$ of $\bar{x}_s$ is 0.9973 (i.e., high probability).

Since measurements are to be made at discrete times, the jth shock foot location x_{sj} is given by $x_{sj} = \bar{x}_s + \Delta x_{sj}$, where Δx_{sj} is the shock foot displacement from $\bar{x}_s$ (see Fig. 6) and is given by $\Delta x_{sj} = \lambda d_j$, where d_j is a Gaussian random variable with zero mean and variance $\sigma_d^2 = (1/n)^2$ (since the mathematical expectation of $\Delta x_{sj}^2 = \lambda^2 d_j^2$ is $\sigma_{xs}^2 = \lambda^2\sigma_d^2$ and since $\lambda = n\sigma_{xs}$). Note that a given sequence of x_{sj} values does not model the time-dependent motion

Table 1 References and experimental conditions

Test configuration	Reference no.	Test parameters	M_∞	δ_o
Blunt fin	13	$D = 0.75$ in.	4.95	0.25, 0.59 in.
	7	$D = 0.50$ in.	2.95	0.13, 0.50 in.
	18	$D = 0.50$ in.	2.95	0.13, 0.50 in.
Compression ramp	14	$\alpha = 28$ deg	4.95	0.76 in.
	15	$\alpha = 28$ deg	4.95	0.59 in.
	20	$\alpha = 24$ deg	2.95, 2.90	0.49,0.87 in.
Cone frustum	19	$\theta_c = 45$ deg	1.6, 2.0, 2.5	0.612, 0.618, 0.635 in.
Incident shock	4	$\theta_w \approx 4.5, 9.5$ deg	3.82, 3.89	7 mm

of x_s but instead models the probability density distribution of x_s between UI and S. It is assumed that the processes modeled here are ergodic.

Figure 6 shows a total of four $\mathcal{P}_i$ samples obtained using four different d_j values. The corresponding pressure levels sensed at station x are P_1, P_2, P_3, and P_4. The mean (or time-averaged) pressure is simply

$$\bar{P}_W(x) = \frac{1}{N}\sum_{k=1}^{N} P_k(x)$$

and the variance is given by

$$\sigma^2_{Pw}(x) = \frac{1}{N-1}\sum_{k=1}^{N}[P_k(x) - \bar{P}_W(x)]^2$$

(for Fig. 6, $N = 4$). Of course, to obtain converged estimates of $\bar{P}_W(x)$ and $\sigma^2_{Pw}(x)$, a sufficiently large number of pressure values are required (i.e., large N). For this study, a value of $N = 200$ was sufficient. In practice, the pressure P_j at any given station x is obtained as $P_j(x) = \mathcal{P}_i(x - \Delta x_{sj}) = \mathcal{P}_i(x - \lambda d_j)$ where $\mathcal{P}_i(x)$ is the $\mathcal{P}_i$ distribution obtained by fixing x_s at $\bar{x}_s$. This produces the same result as the preceding conceptual approach. When $\bar{P}_W(x)$ values are available at discrete values only (as from experiment), linear interpolation is used to obtain intermediate values of $\mathcal{P}_i$.

The steps in the method are summarized as follows:

Set $\mathcal{P}_i(x) = \bar{P}_W(x)$.
Set $\lambda = \delta_o$ for two-dimensional interactions,
  $= D$ for hemicylindrical leading-edge blunt fins.
Loop over Nd_j values ($j = 1, N$),
  choose d_j,
  loop over each x value,

$$P_j(j, x) = \mathcal{P}_i(x - \lambda d_j)$$

  end of x loop.
End of d_j loop.
Calculate $\bar{P}_W(x)$ and $\sigma_{Pw}(x)$.

Results

Fluctuating wall pressure measurements (in interactive flows) have been reported in the open literature for primarily five model configurations. They are cylinders and blunt fins (with various leading-edge shapes and leading-edge sweep angles), sharp fins at angle of attack, cone-frustum configurations, swept and unswept compression corners, and incident shocks. In addition, one study has been made of fluctuating heat transfer levels associated with incident shocks. This paper makes use of those cases for which the actual statistical values (mean, standard deviation) were available or could be obtained by digitizing data figures presented in the literature. The respective references (and flow conditions) are provided in Table 1. In this paper, only separated flow cases will be discussed. Reference 17 provides additional results, including cases of unseparated interactions. Descriptions of the facilities and models can be found in the respective references. In the discussions that follow, the magnitude of the upstream-most maximum in the experimentally measured wall pressure standard deviation distribution will be referred to as $\sigma_{\max,1}$. The successive minima and maxima downstream of $\sigma_{\max,1}$ will be similarly denoted as $\sigma_{\min,1}$, $\sigma_{\max,2}$, and so on. For the Mach 5 blunt fin data set (Fig. 3), the uncertainties in the measured values of mean wall pressure and fluctuating pressure standard deviation at the x location corresponding to $\sigma_{\max,1}$ are estimated to be $\bar{P}_W = 1.20 \pm 0.05$ psia and $\sigma_{Pw} = 0.30 \pm 0.01$ psia.

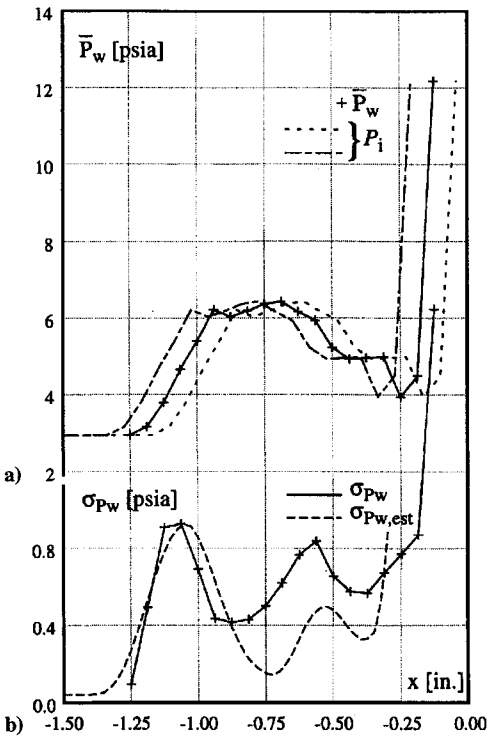

Fig. 7 Mach 3 blunt fin centerline a) pressure distributions and b) measured and estimated standard deviation distributions.

Hemicylindrically Blunted Fins

The mean pressure $[\bar{P}_W(x)]$ and pressure standard deviation $[\sigma_{Pw}(x)]$ distributions on centerline ahead of a blunt fin at Mach 3 are shown in Figs. 7a and 7b. The data are from the study by Dolling and Bogdonoff.[7] For this case, $D = 0.5$ in. and $\delta_o = 0.13$ in. Note how the two upstream maxima in $\sigma_{Pw}(x)$ correlate with steep sloping portions of $\bar{P}_W(x)$ whereas the two minima downstream of $x = -1$ in. correspond to relatively flat portions of $\bar{P}_W(x)$, respectively. As described earlier, the low-frequency contributions to $\sigma_{Pw}(x)$ [i.e., $\sigma_{LP}(x)$ in Fig. 3b] are due primarily to the large-amplitude, low-frequency motion of $\mathcal{P}_i$. Estimates of $\sigma_{LP}(x)[\sigma_{LP,est}(x)]$ are made by first using $\bar{P}_W(x)$ to approximate the spatial distribution of $\mathcal{P}_i$. Then, a set of 200 $\mathcal{P}_i$ distributions are obtained using a normally distributed set of shock foot displacements, where the length of the region of shock motion, λ, is approximated using the fin diameter (i.e., $\lambda \approx D$). In Fig. 7a (and most of the other examples that follow), sample $\mathcal{P}_i$ distributions are shown for $\Delta x_{sj} = \pm 1\sigma_{xs}$ to illustrate the extent of shock motion. Note the similarity to Fig. 2a of the present paper and Fig. 13 of Ref. 12.

Using the 200 distributions, we calculated $\sigma_{Pw,est}$. The result is shown in Fig. 7b. As seen, the shape of $\sigma_{Pw,est}(x)$ agrees with that of $\sigma_{Pw}(x)$. In addition, the magnitude of $\sigma_{\max,1}$ is extremely well predicted (for $N = 200$, the estimated value of $\sigma_{\max,1}$ has an

uncertainty of ±7%; increasing N to 500 reduces the uncertainty only to ±4.2%). If the original experimental data could be digitally filtered, similar to what was done to obtain Fig. 3b, then the accuracy of the estimated value of $\sigma_{\max,2}$ (Fig. 7b) could also be determined. However, the original pressure signals were unavailable. Toward the root, the slope of $\sigma_{Pw,\,est}$ appears to match the slope in the experimental data. However, due to the difficulty in resolving the pressure measurements spatially [due to the steep gradients in $\bar{P}_W(x)$ and $\sigma_{Pw}(x)$ near the root], as well as to uncertainty of length of $\mathcal{P}_i$ motion near the root, this agreement may be fortuitous. A second experiment done at Mach 3 used a thicker boundary layer ($D = 0.5$ in. and $\delta_o = 0.5$ in.). The shape of $\sigma_{Pw,\,est}$ (not shown) agreed with the shape of $\sigma_{Pw}(x)$, but the magnitude of $\sigma_{\max,1}$ was underpredicted by about 25%.

Computations of the preceding two Mach 3 flows have been made by Hung and Buning.[18] Figure 8a shows $\bar{P}_W(x)$ obtained from computation and experiment for the case of $D = 0.5$ in. and $\delta_o = 0.13$ in. The computation agrees fairly well with experiment, although the predicted upstream maximum is roughly 20% too large, and the downstream minimum is underpredicted. The estimated standard deviation distribution obtained using the computed mean pressure distribution is shown in Fig. 8b and agrees well with the shape of $\sigma_{Pw}(x)$. Although the predicted location of $\sigma_{\max,1}$ is slightly downstream of the measured location, the magnitude of $\sigma_{\max,1}$ is well predicted. The second maximum ($\sigma_{\max,2}$) is overpredicted because, as seen in Fig. 8a, the drop in pressure in the mean distribution between $x = -0.8$ and -0.5 in. is significantly larger in the computation than in the experiment. For the second case (not shown), for which δ_o is larger ($D = 0.5$ in. and $\delta_o = 0.5$ in.), the computed mean pressure distribution also agrees fairly well with the measurements. The upstream maximum and downstream minimum in the experimentally measured $\bar{P}_W(x)$ distribution are again overpredicted (by about 10%) and underpredicted, respectively, in the computation. Similarly, the predicted location of $\sigma_{\max,1}$ is slightly downstream of the measured location. Also, the magnitude of $\sigma_{\max,1}$ is underestimated by about 20%. The magnitude of $\sigma_{\max,1}$, however, agrees more closely with the measured value than does the level predicted using the experimentally obtained mean pressure distribution.

In addition to the preceding Mach 3 studies, blunt fin data of Brusniak[13] at Mach 5 were examined for $D = 0.75$ in. with $\delta_o = 0.59$ and 0.25 in. For both cases of δ_o, the shapes of $\sigma_{Pw,\,est}(x)$ agree with the corresponding $\sigma_{Pw}(x)$ distributions (see Fig. 8 of Ref. 17). The magnitudes of the corresponding $\sigma_{\max,1}$ values, however, were less well predicted than for the Mach 3 data sets (up to 45% underprediction for the $\delta_o = 0.59$ in. case); however, the prediction is better for the thinner boundary-layer case (roughly 25% underpredicted).

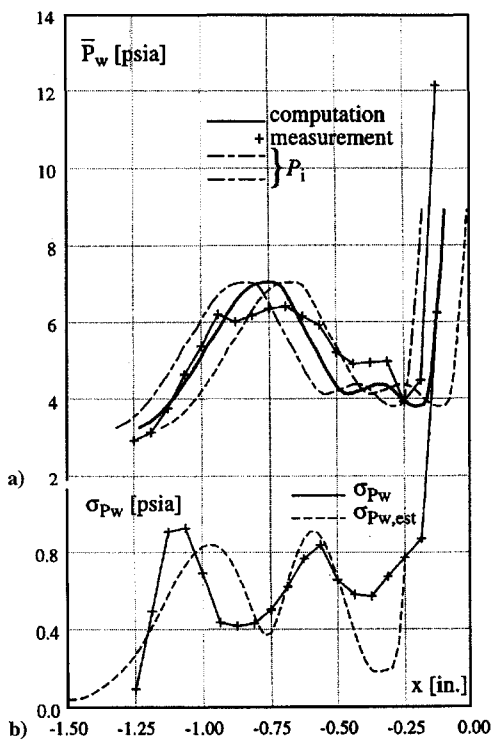

Fig. 8 Mach 3 blunt fin a) measured and computed mean pressure distributions and b) measured and estimated standard deviation distributions.

Ogive-Cylinder Cone-Frustum Configuration

Figure 9a shows the experimental configuration used by Chyu and Hanly[19] at Mach numbers of 1.6, 2, and 2.5 for their ogive-cylinder cone-frustum configuration. The mean pressure distributions are presented in Fig. 9b as $\bar{P}_W(x) - P_\infty$. Qualitatively, the expectation is that a maximum in $\sigma_{Pw}(x)$ will occur at about $x = -8$ in. for all cases since the slopes of the mean pressure distributions are maximum (i.e., points of inflection) near there. This is indeed the case, as shown by the $\sigma_{Pw}(x)$ distributions in Figs. 9c–9e. Note from Table 1 that δ_o (hence, λ) is roughly the same for all three cases. Also shown in the figures are the corresponding $\sigma_{Pw,\,est}(x)$ distributions obtained using $\lambda = \delta_o$. As seen, as the overall levels of $\bar{P}_W(x) - P_\infty$ decrease (from about 2.5 to 1, Fig. 9b), the corresponding estimates of $\sigma_{\max,1}$ decrease in accuracy, from excellent for $M_\infty = 1.6$ [note that the upstream maximum in $\sigma_{Pw}(x)$ is not well resolved experimentally] to about 40% underpredicted for $M_\infty = 2.5$. An explanation of this trend will be given later. The locations of the maxima are very well predicted.

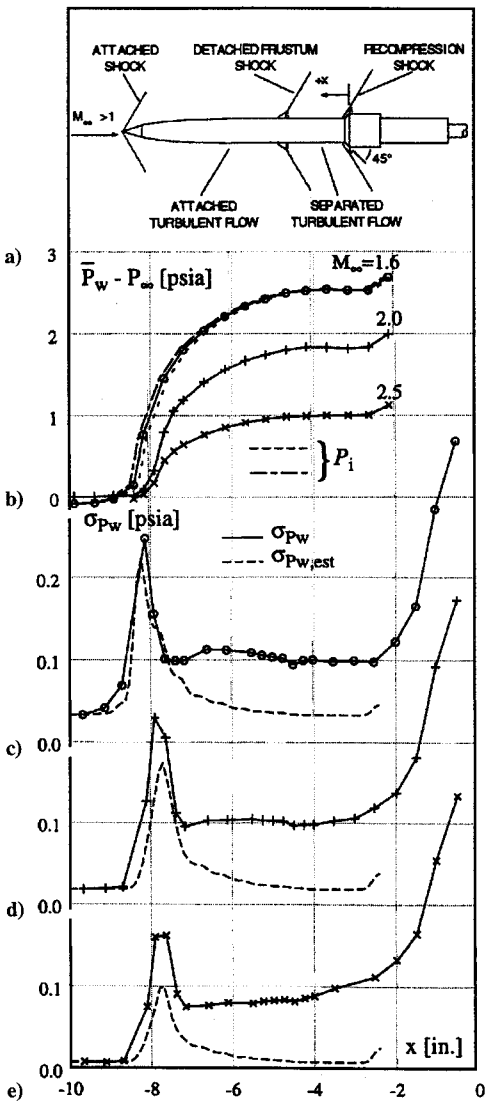

Fig. 9 Cone-frustum a) experimental configuration; b) mean pressure distributions; and measured and estimated standard deviation distributions for c) $M_\infty = 1.6$; d) $M_\infty = 2.0$; and e) $M_\infty = 2.5$.

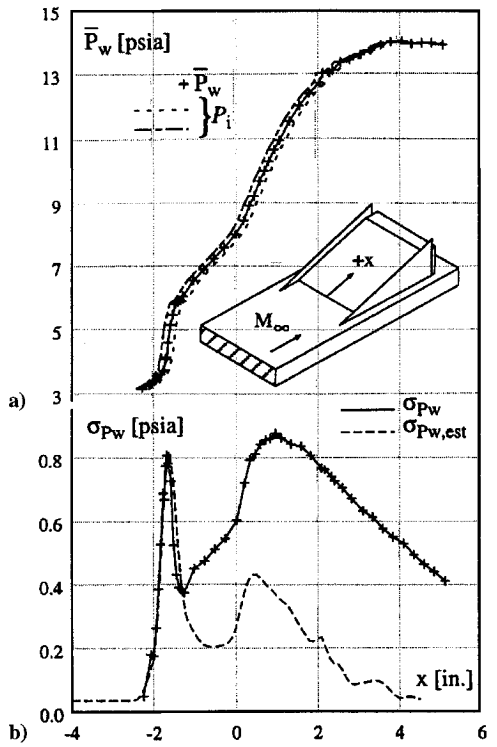

Fig. 10 Mach 3 compression ramp (α = 24 deg) experimental configuration (inset) and a) mean pressure distribution and b) measured and estimated standard deviation distributions.

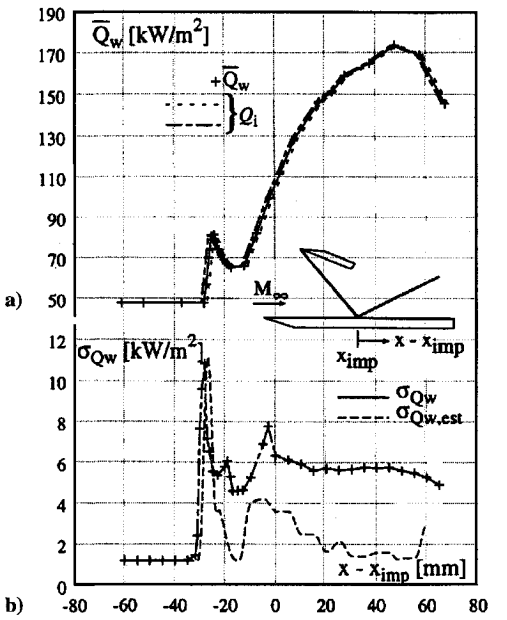

Fig. 11 Mach 3.89 incident shock experimental configuration (inset) and a) mean heat flux distribution and b) measured and estimated heat flux standard deviation distributions.

Compression Corners

The inset in Fig. 10 shows the experimental setup used by Dolling and Murphy[20] at Mach 3. Measurements were taken using a ramp angle of $\alpha = 24$ deg with $\delta_o = 0.87$ in. Comparing $\bar{P}_W(x)$ (Fig. 10a) with $\sigma_{Pw}(x)$ (Fig. 10b), it is clear that the steep slopes in $\bar{P}_W(x)$ near $x = -1.5$ in. and between $x = 0$ and 2 in. correlate with the respective maxima in $\sigma_{Pw}(x)$ and that the less steep slope in $\bar{P}_W(x)$ between $x = -1.25$ and 0 in. correlates with the respective minimum in $\sigma_{Pw}(x)$. Using $\lambda = \delta_o$, the upstream maximum in $\sigma_{Pw,\,est}(x)$ matches the corresponding maximum in $\sigma_{Pw}(x)$ extremely well, in terms of location and magnitude. Again, if the original pressure signals could be digitally filtered, similar to what was done to obtain Fig. 4b, then the accuracy of the maximum in $\sigma_{Pw,\,est}(x)$ downstream of the corner ($x > 0$) could be determined. An additional set of data (from Ref. 20) using $\alpha = 24$ deg, but with a thinner boundary layer ($\delta_o = 0.49$ in.) was also examined. In this case, the agreement between $\sigma_{Pw,\,est}(x)$ and $\sigma_{Pw}(x)$ was of the same quality as for the preceding case with $\delta_o = 0.87$ in. Using compression corner data (from Ref. 15) at Mach 5 ($\alpha = 28$ deg), $\sigma_{Pw,\,est}(x)$ was qualitatively the same shape as the corresponding $\sigma_{Pw}(x)$ distribution, but $\sigma_{\max,1}$ was underestimated by about 30%.

Incident Shocks

The inset in Fig. 11 shows the experimental configuration used by Hayashi et al.[4] Incident shock waves with angles of 18.5 and 22.3 deg at Mach 3.82 and 3.89, respectively, were used to generate unseparated and separated flows, respectively. This study is unusual in that fluctuating heat transfer measurements were made. As noted in the study, the character of the fluctuating heat transfer signals from the region of shock motion bore a close resemblance to the character of fluctuating pressure signals taken from the same region. Using this observation, the assumption is made that an instantaneous heat transfer distribution $\mathcal{Q}_i$ (analogous to $\mathcal{P}_i$) exists and that the time-averaged heat transfer distribution $\bar{Q}_W$ can be used to approximate the shape of $\mathcal{Q}_i$; that is, that $\mathcal{Q}_i(x) \approx \bar{Q}_W(x)$. Following the same procedure as used for $\mathcal{P}_i$, an estimated standard deviation distribution of the fluctuating heat transfer levels, $\sigma_{Qw,\,est}$, can be obtained and compared with the actual distribution, $\sigma_{Qw}(x)$. In this case, $\sigma_{Qw,\,est}$ is assumed to correspond to low-frequency motion of $\mathcal{Q}_i$. This assumption would have to be confirmed by experiment.

Figure 11a shows $\bar{Q}_W(x)$ for the case of separated flow (see Ref. 18 for a discussion of the unseparated flow case). Based on the shape of $\bar{Q}_W(x)$, $\sigma_{Qw}(x)$ would be expected to have a local maximum at about $x - x_{\text{imp}} = -30$ mm [region of large slope in $\bar{Q}_W(x)$] followed by a minimum near $x - x_{\text{imp}} = -25$ mm (region of zero slope), a maximum between $x - x_{\text{imp}} = -25$ and about -15 mm, a minimum near $x - x_{\text{imp}} = -15$ mm, and another maximum between $x - x_{\text{imp}} = -10$ and $+20$ mm. Comparison with $\sigma_{Qw}(x)$ in Fig. 11b shows that this is the case. Also shown in Fig. 11b is $\sigma_{Qw,\,est}(x)$ obtained using $\lambda = \delta_o$. The locations of the three maxima in $\sigma_{Qw,\,est}(x)$ are predicted well in $\sigma_{Qw,\,est}(x)$, and the magnitude of the upstream-most maximum in $\sigma_{Qw}(x)$ is very well predicted.

Discussion of Results

Qualitatively, in all of the cases examined, the shape of the measured standard deviation distributions (i.e., the locations of local maxima and minima) could be inferred from the character of the corresponding mean distributions and was predicted correctly in the estimated standard deviation distributions. To first order, regions of large gradient in the mean distribution (usually, at points of inflection) correspond to local maxima in the corresponding standard deviation distribution, and regions of small gradient correspond to local minima. This is not meant to imply that local values of standard deviation are in general mathematically proportional to the local gradient in the mean distribution, because local maxima and minima in the mean distribution would imply standard deviation values of exactly zero. In reality, σ_{Pw}, for example, is largely a measure of local changes in pressure that occur as $\mathcal{P}_i$ moves about. At a point, σ_{Pw} is a function of the shape of the local portion of $\mathcal{P}_i$ [which is related to the gradient in $\bar{P}_W(x)$] centered about the measurement point.

Quantitatively, some of the major observations of the estimated magnitude of $\sigma_{\max,1}$ using experimentally and computationally obtained mean distributions are as follows.

Blunt fins: Estimates ranged from a worst case 45% underprediction for the Mach 5 data to excellent for Mach 3; further, for both Mach numbers, the estimates associated with thinner boundary layers were more accurate than for thicker boundary layers.

Cone-frustum: Estimates ranged from 40% underprediction to good, with accuracy decreasing with decreasing overall absolute pressure difference across the separation shock.

Compression corner: The Mach 5 levels ($\alpha = 28$ deg) were underestimated by about 30%, whereas the Mach 3 levels ($\alpha = 24$ deg) were predicted extremely well.

Incident shock: The fluctuating heat transfer levels were predicted extremely well.

Overall, excellent estimates of the magnitude of $\sigma_{\max,1}$ were obtained for the Mach 3 blunt fin, Mach 3 compression corner, and Mach 3.89 incident shock cases shown in Figs. 7, 10, and 11, respectively. Recall Eq. (2). As discussed in the Method section, when a given segment of $\mathcal{P}_i(x)$ is linear, a corresponding segment of $\bar{P}_W(x)$ will also be linear and in fact equal to $\mathcal{P}_i(x)[\bar{P}_W(x) \approx \mathcal{P}_i(x)]$. In each of the aforementioned figures, the locations of $\sigma_{\max,1}$ correlate, respectively, with portions of their corresponding mean distributions, which are quite linear.

For the cone-frustum data (Fig. 9), the magnitude of $\sigma_{\max,1}$ (i.e., near $x = -8$ in.) is increasingly underestimated as the pressure difference across the separation shock decreases. [Note that since the boundary-layer thickness is essentially the same for all cases (see Table 1), this implies that λ is also the same for all cases.] In addition, the location of $\sigma_{\max,1}$ for all three cases does not have corresponding distinct linear portions in the mean distributions as was seen in the earlier examples. This implies that each $\mathcal{P}_i$ distribution has some degree of concavity, that the approximation $\mathcal{P}_i(x) \approx \bar{P}_W(x)$ will be less accurate, and that some difference will exist between the actual and estimated maxima in $\sigma_{P_W}(x)$. Also, as the pressure difference across the separation shock decreases, the concavity of the upstream portion ($x < -7$ in.) of the mean distributions appears to correspondingly increase, implying that the accuracy of the estimated value of $\sigma_{\max,1}$ would correspondingly decrease, as does occur.

One additional point is the observation for the blunt fin flows that, for a given fin configuration, the accuracy of the standard deviation distribution estimates improved as the undisturbed boundary-layer thickness was reduced. From the study by Dolling and Smith[8] it has been shown that, for a fixed fin diameter, decreasing the oncoming turbulent boundary-layer thickness results in a second-order decrease in shock foot length of motion. That is, λ is actually of a form $\lambda \approx D + fn(\delta_o)$, where the contribution from $fn(\delta_o)$ is of second order compared with the contribution from D. In light of the form of Eq. (2), a decrease in boundary-layer thickness would result in a decrease in λ. This would consequently improve the accuracy of the approximation $\mathcal{P}_i(x) \approx \bar{P}_W(x)$ and would improve the accuracy of the standard deviation distribution estimates. This behavior is consistent with the observed results.

In summary, the accuracy of the standard deviation distribution estimates appears to depend primarily on two factors: the shape of $\mathcal{P}_i(x)$ and the length of the region of shock foot motion λ. When a given segment of $\mathcal{P}_i(x)$ is linear, $\bar{P}_W(x)$ will be equal to $\mathcal{P}_i(x)$ over a corresponding segment, and the corresponding portion of the estimated standard deviation distribution will be accurate. On the other hand, when $\mathcal{P}_i(x)$ is nonlinear (i.e., has concavity), the accuracy of the approximation $\bar{P}_W(x) \approx \mathcal{P}_i(x)$ decreases and the accuracy of the estimated standard deviation distribution also decreases. Both of these points were evident in all of the results (including those not shown). The effect of increasing λ is to increase the contribution of the second-order and higher derivative terms in Eq. (2) to the mean value, likewise decreasing the accuracy of both the approximation $\bar{P}_W(x) \approx \mathcal{P}_i(x)$ and the estimated standard deviation distribution. This trend was evident in the blunt fin results.

Conclusions

Mean wall pressure (and mean wall heat transfer) distributions can be used to make first-order estimates of the magnitude (and distribution of magnitude) of fluctuating wall pressures (and fluctuating heat transfer) in a broad range of flows involving shock wave/turbulent boundary-layer interactions. The method provides an important tool for designers of high-speed vehicles since first-order estimates of the location and magnitude of surface loads can be obtained simply, using either measured or computed mean distributions. It is especially important because it will likely be several years before fully time-dependent, three-dimensional, interactive turbulent flow computations can be done on a routine basis. The method may also prove useful in the planning of experiments. For example, if the goal of an experimental program is to determine which of a large number of model geometries generates the largest fluctuating load levels, then mean pressure distributions could be measured (or computed) first for all models and then used to generate loading level estimates for all cases. From these estimates, the best candidates for intensive time series measurements could be selected, thereby reducing the cost of the program. The most critical factors affecting the accuracy of the estimates appear to be the shape of the instantaneous pressure (heat transfer) distribution and the length of the region of shock foot motion.

Acknowledgments

This work was supported by the Applied Research Laboratories Independent Research and Development program. This source of support is gratefully acknowledged. The authors gratefully acknowledge the reviewer of this paper who suggested the analytical approach that led to Eq. (2).

References

[1]Holden, M. S., "A Review of Aerothermal Problems Associated with Hypersonic Flight," AIAA Paper 86-0267, Jan. 1986.

[2]Dolling, D. S., "Fluctuating Loads in Shock Wave/Turbulent Boundary Layer Interaction: Tutorial and Update," AIAA Paper 93-0284, Jan. 1993.

[3]Pozefsky, P., Blevins, R. D., and Laganelli, A. L., "Thermo-Vibro-Acoustic Loads and Fatigue of Hypersonic Flight Vehicle Structures," U.S. Air Force Wright Aeronautical Labs., AFWAL TR-89-3014, Wright–Patterson AFB, OH, Feb. 1989.

[4]Hayashi, M., Aso, S., and Tan, A., "Fluctuation of Heat Transfer in Shock Wave/Turbulent Boundary-Layer Interaction," *AIAA Journal*, Vol. 27, No. 4, 1989, pp. 399–404.

[5]Brown, J. D., Brown, J. L., Kussoy, M. I., Holt, M., and Horstmann, C. C., "Two-Component LDV Investigation of Three-Dimensional Shock Boundary-Layer Interaction," *AIAA Journal*, Vol. 26, No. 1, 1988, pp. 52–56.

[6]Dolling, D. S., and Brusniak, L., "Correlation of Separation Shock Motion in a Cylinder-Induced Interaction with Pressure Fluctuations Under the Separated Region," AIAA Paper 91-0650, Jan. 1991.

[7]Dolling, D. S., and Bogdonoff, S. M., "An Experimental Investigation of the Unsteady Behavior of Blunt Fin-Induced Shock Wave Turbulent Boundary Layer Interactions," AIAA Paper 81-1287, June 1981.

[8]Dolling, D. S., and Smith, D. R., "Separation Shock Dynamics in Mach 5 Turbulent Interactions Induced by Cylinders," *AIAA Journal*, Vol. 27, No. 12, 1989, pp. 1698–1706.

[9]Keefe, L. R., and Nixon, D., "Shock Loading Predictions from Application of Indicial Theory to Shock-Turbulence Interactions," AIAA Paper 91-1777, June 1991.

[10]Debieve, J. F., and Lacharme, J. P., "A Shock-Wave/Free Turbulence Interaction," *Proceedings of IUTAM Symposium in Turbulent Shear Layer-Shock Wave Interactions*, Springer–Verlag, New York, 1986, pp. 393–403.

[11]Laganelli, A. L., and Wolfe, H. F., "Prediction of Fluctuating Pressure in Attached and Separated Turbulent Boundary-Layer Flow," *Journal of Aircraft*, Vol. 30, No. 6, 1993, pp. 962–970.

[12]Brusniak, L., and Dolling, D. S., "Physics of Unsteady Blunt-Fin Induced Shock Wave/Turbulent Boundary Layer Interactions," *Journal of Fluid Mechanics*, Vol. 273, Aug. 1994, pp. 375–409.

[13]Brusniak, L., "Physics of Unsteady Blunt-Fin Induced Shock Wave/Turbulent Boundary Layer Interactions," Ph.D. Dissertation, Dept. of Aerospace Engineering and Engineering Mechanics, Univ. of Texas, Austin, TX, May 1994.

[14]Barter, J. W., and Dolling, D. S., "Reduction of Fluctuating Pressure Loads in Shock Wave Turbulent Boundary Layer Interactions," AIAA Paper 95-0673, Jan. 1995.

[15]Erengil, M. E., and Dolling, D. S., "Unsteady Wave Structure near Separation in a Mach 5 Compression Ramp Interaction," *AIAA Journal*, Vol. 29, No. 5, 1991, pp. 728–735.

[16]Erengil, M. E., and Dolling, D. S., "Effects of Sweepback on Unsteady Separation in Mach 5 Compression Ramp Interactions," *AIAA Journal*, Vol. 31, No. 2, 1993, pp. 302–311.

[17]Brusniak, L., and Dolling, D. S., "Engineering Approach to the Estimation of Fluctuating Loads in Shock Wave/Turbulent Boundary-Layer Interactions," AIAA Paper 95-1802, June 1995.

[18]Hung, C.-M., and Buning, P. E., "Simulation of Blunt Fin-Induced Shock Wave and Turbulent Boundary Layer Interaction," *Journal of Fluid Mechanics*, Vol. 154, May 1985, pp. 163–185.

[19]Chyu, W. J., and Hanly, R. D., "Power- and Cross-Spectra and Space-Time Correlations of Surface Fluctuating Pressures at Mach Numbers Between 1.6 and 2.5," NASA TN D-5440, Sept. 1969.

[20]Dolling, D. S., and Murphy, M. T., "Unsteadiness of the Separation Shock Wave Structure in a Supersonic Compression Ramp Flowfield," *AIAA Journal*, Vol. 21, No. 12, 1983, pp. 1628–1634.